Scalarization of isolated black holes in scalar Gauss-Bonnet theory in the fixing-the-equations approach

Guillermo Lara,[1,*] Harald P. Pfeiffer,[1] Nikolas A. Wittek,[1] Nils L. Vu,[2] Kyle C. Nelli,[2] Alexander Carpenter,[3] Geoffrey Lovelace,[3] Mark A. Scheel,[2] and William Throwe[4]

[1]*Max Planck Institute for Gravitational Physics (Albert Einstein Institute), Am Mühlenberg 1, 14476 Potsdam, Germany*

[2]*Theoretical Astrophysics, Walter Burke Institute for Theoretical Physics, California Institute of Technology, Pasadena, California 91125, USA*

[3]*Nicholas and Lee Begovich Center for Gravitational-Wave Physics and Astronomy, California State University Fullerton, Fullerton, California 92831, USA*

[4]*Cornell Center for Astrophysics and Planetary Science, Cornell University, Ithaca, New York 14853, USA*

(Received 22 March 2024; accepted 14 June 2024; published 15 July 2024)

One of the most promising avenues to perform numerical evolutions in theories beyond general relativity is the *fixing-the-equations* approach, a proposal in which new "driver" equations are added to the evolution equations in a way that allows for stable numerical evolutions. In this direction, we extend the numerical relativity code SpECTRE to evolve a "fixed" version of scalar Gauss-Bonnet theory in the decoupling limit, a phenomenologically interesting theory that allows for hairy black hole solutions in vacuum. We focus on isolated black hole systems both with and without linear and angular momentum, and propose a new driver equation to improve the recovery of such stationary solutions. We demonstrate the effectiveness of the latter by numerically evolving black holes that undergo spontaneous scalarization using different driver equations. Finally, we evaluate the accuracy of the obtained solutions by comparing with the original unaltered theory.

DOI: 10.1103/PhysRevD.110.024033

I. INTRODUCTION

The increasing availability of gravitational wave (GW) data, by current (LIGO-Virgo-KAGRA [1–3]) and future (LISA [4], Einstein Telescope [5], Cosmic Explorer [6]) ground and space-based interferometers, promises to lead to the strictest tests yet of Einstein's general theory of relativity (GR) as the fundamental description of gravitational phenomena. Adding on to the vast array of weak-field tests [7], a growing suite of model-independent tests on the GW signal from binary compact coalescences (BCCs) [8–10] show no apparent disagreement with GR to date. At the same time, direct observation by means of very-large-baseline interferometry show black hole (BH) images consistent with expectations based on Einstein's gravity [11,12].

Nevertheless, it is conceivable that GR is not the ultimate description of gravity. On the theoretical side, the quantum nature of all matter and force fields in the Standard Model, firmly established in the past half-century, suggests the existence of a quantum theory of gravity. From this perspective, GR arises as an *effective field theory* (EFT) with limited range of applicability and is subject to corrections relevant at shorter (higher) length (curvature) scales. On the phenomenological side, modifying gravity at the largest scales (e.g. by introducing new light degrees of freedom) could help explain cosmological issues such as the observed self-accelerated expansion of the Universe (or dark energy) [13]. Among other motivations, numerous extensions of GR have been devised. Some of the most important classes of theories include degenerate higher-order scalar-tensor theories [14–16]—a generalization of the Horndeski class [17]–and EFT expansions of gravity—see e.g. Refs. [18,19].

It is expected that GW signals will carry information about possible GR corrections. Already, tight constraints on the speed of tensor modes from GW170917 [20,21] have cast widely encompassing constraints on dark energy models [22–25]. However, in order to fully exploit the potential of GWs to cast the strictest bounds on beyond-GR parameters, model-dependent tests need to be carried out for (if only a few) alternative theories of gravity. In this direction, there is a need to construct full waveform models, encompassing all stages of BCC. For GR, numerical

*Contact author: glara@aei.mpg.de

simulations of the late-inspiral and merger phases of compact binary coalescence are essential to construct and calibrate models describing these highly dynamical and nonlinear stages [26–29]. Therefore, a key (and challenging) step is to extend the techniques of numerical relativity (NR) [30] beyond GR.

As it was the case for GR decades ago, one of the main difficulties is the mathematical structure of equations of motion. These systems of partial differential equations (PDEs) need to be recast (if possible) in a way suitable for numerical evolution, such that the system admits a *well-posed* initial-value problem (IVP)—a property that ensures good behavior of the solutions: uniqueness and continuity on the space of initial data [31]. Failure to satisfy this property can give rise to unstable solutions and even seemingly pathological behavior—e.g. hyperbolic PDE systems have been observed to change character to elliptic in regions outside BH horizons [32–40]. Nevertheless, recent developments have fuelled renewed interest and a steady increase in beyond-GR codes and GW-waveform examples—see Ref. [41] for a review. Indeed, some of us have obtained beyond-GR waveforms in dynamical Chern-Simons and scalar Gauss-Bonnet (sGB) theory using an order-reduction scheme to obtain perturbative corrections to the GW signal [42–45]—see also Refs. [46–48]. Other studies have adopted theory-specific approaches, in some cases involving explorations of the beyond-GR parameter space [49–56]. More recently, novel modified generalized harmonic (GH) gauges applicable for a broad class of weakly coupled Lovelock and Horndeski theories have been proposed by Kovacs and Reall [57,58]. The latter have been numerically implemented in Refs. [32,59,60], as well as in similar extensions to the conformal and covariant Z4 (CCZ4) system [61,62], to evolve binary systems in sGB EFTs.

Here we will explore a fourth avenue, sometimes referred to in the literature as the *fixing-the-equations* approach [63]. In this proposal (inspired by Müller-Israel-Stewart hydrodynamics), the equations of motion are deformed (or "fixed") by the introduction of auxiliary variables subject to suitable *driver* evolution equations. New timescales appearing in these driver equations control how the fixed solutions track the solutions of the original system, thus allowing for the evolution of the scales relevant to the problem, while "softening" (possibly) problematic high-frequency modes.

In this paper, we report on the first steps to implement the fixing-the-equations approach in the numerical relativity code SpECTRE [64], developed by the SXS Collaboration. While this method can be applied to a wide variety of theories (see e.g. Refs. [52,65–70]), for concreteness and motivated by positive results in spherical symmetry [68], we will focus on sGB gravity in vacuum. The action is

$$S[g_{ab},\Psi] \equiv \int d^4x\sqrt{-g}\left[\frac{R}{2\kappa}-\frac{1}{2}(\nabla_a\Psi\nabla^a\Psi)+\ell^2 f(\Psi)\mathcal{G}\right], \tag{1}$$

where $\kappa \equiv 1/(8\pi G)$ and ℓ are constant couplings, $g = \det(g_{ab})$ is the determinant of the metric g_{ab}, the scalar field is Ψ, $f(\Psi)$ is a free function describing the specific coupling to the Gauss-Bonnet scalar

$$\mathcal{G} \equiv R_{abcd}R^{abcd} - 4R_{ab}R^{ab} + R^2, \tag{2}$$

which is defined in terms of combinations of the Riemann tensor R_{abcd}, the Ricci tensor R_{ab} and the Ricci scalar R. Scalar Gauss-Bonnet theory is of phenomenological interest mainly because it is a model for black holes endowed with scalar *hair* [71,72]. As opposed their GR counterparts (described by the Kerr metric [73]), BHs in sGB theory evade common no-hair theorems [74–77] and are characterized by a *scalar charge* in addition to their mass and spin parameters. BHs can acquire scalar hair through a variety of *scalarization* mechanisms (see Ref. [78] for a review) and it is expected that this hair will significantly impact the GW signal from binary black hole (BBH) systems. Recently, model-dependent bounds using the inspiral phase of GW observations have been placed on shift-symmetric sGB models—giving values of $\ell \lesssim \mathcal{O}(1)$ km [79,80]. Additional theoretical constraints on the form of the coupling function $\ell^2 f(\Psi)$ have been derived from the assumption of consistency of sGB theory with a well-behaved (high energy) ultraviolet completion [81].

In our implementation of the fixing-the-equations approach, we consider the following (related) issues: (i) Can we accurately describe the stationary solutions of the theory? (ii) Can we be confident that the fixed equations are able to reproduce the original physics? We address both questions empirically in a case study: the scalarization of isolated BHs in the *decoupling limit* of theory (1)—where the scalar field backreaction on the metric is neglected. The reason why this approximation is illustrative is twofold. First, it will help us test the properties of different driver equations in a localized sector: the scalar sector. Second, the "unmodified" decoupled theory can be recast in strongly hyperbolic form and thus readily evolved so as to compare different "fixing" prescriptions against the "correct" solution. Finally, as a main result of this paper, we present a new driver equation that leads to an improved recovery of the stationary solutions of the theory, with respect to other equations studied in the literature–see Fig. 2.

This paper is organized as follows. In Sec. II, we give a brief theoretical background of sGB theory and the fixing-the-equations approach. We describe our numerical implementation and diagnostics in Sec. III. In Sec. IV, we illustrate with different examples of isolated BH scalarization how stationary solutions are recovered by the fixed systems and how the new driver equation improves their accuracy using a variety of diagnostics. We summarize our results and comment on the future steps of this program in Sec. V. Further material is presented in the Appendices. In Appendix A the driver equations of the main text are compared with a third

wavelike driver. Finally, in Appendix B, convergence plots are presented. Throughout this paper we set $G = c = 1$ and work in $-+++$ signature. Early alphabet letters $\{a, b, c, \ldots\}$ represent 4-dimensional spacetime indices, whereas middle letters $\{i, j, k, \ldots\}$ represent 3-dimensional spatial indices.

II. THEORY

Taking the variation of action (1) with respect to the scalar field Ψ, we obtain the scalar equation

$$\Box\Psi = -\ell^2 f'(\Psi)\mathcal{G}. \tag{3}$$

Variation with respect to the metric yields

$$G_{ab} = \kappa(T^{(\Psi)}_{ab} + \ell^2 H_{ab}), \tag{4}$$

where $G_{ab} \equiv R_{ab} - (R/2)g_{ab}$ is the Einstein tensor,

$$T^{(\Psi)}_{ab} \equiv \nabla_a\Psi\nabla_b\Psi - \frac{1}{2}g_{ab}\nabla_c\Psi\nabla^c\Psi \tag{5}$$

is the canonical stress-energy tensor of the scalar, and [68]

$$H_{ab} \equiv -8P_{acbd}\nabla^c\nabla^d f(\Psi), \tag{6}$$

with

$$P_{abcd} \equiv R_{abcd} - 2g_{a[c}R_{d]b} + 2g_{b[c}R_{d]a} + g_{a[c}g_{d]b}R. \tag{7}$$

In the *decoupling limit* of the theory, the backreaction of the scalar field on Eq. (4) is neglected. The resulting system is equivalent to a test scalar field, described by Eq. (3), which evolves on a known GR background (see e.g. [47,48]):

$$\Box\Psi = -\ell^2 f'(\Psi)\mathcal{G} \qquad R_{ab} = 0. \tag{8}$$

A. Spontaneous scalarization

In order to describe BHs that undergo *spontaneous scalarization*, we will consider the model of Ref. [82]

$$f(\Psi) \equiv \frac{\eta}{8}\Psi^2 + \frac{\zeta}{16}\Psi^4, \tag{9}$$

where η and ζ are dimensionless parameters. As can be readily seen from Eq. (9) and action (1), the resulting theory is $\mathbb{Z}_2$ symmetric and solutions related by $\Psi \to -\Psi$ are equivalent.

A trivial solution to Eqs. (3) and (4) is a Kerr metric with $\Psi \equiv 0$. Thus, the solutions of GR are also solutions for model (9) of sGB theory. Nevertheless, a *tachyonic* instability in the scalar sector may render GR solutions linearly unstable [78]. This can be readily seen in the decoupling limit by writing the equation for a linear perturbation $\Psi = \delta\Psi + \mathcal{O}(\delta\Psi^2)$ of the scalar, which reads

$$(\Box - m^2_{\Psi,\mathrm{eff}})\delta\Psi = 0 \tag{10}$$

where $m^2_{\Psi,\mathrm{eff}} \equiv -\ell^2 f''(\Psi)\mathcal{G}|_{\Psi=0} = -\ell^2\eta\mathcal{G}/4$. Depending on the combined signs of the coupling η and the Gauss-Bonnet scalar $\mathcal{G}$, unstable regions where $m^2_{\Psi,\mathrm{eff}} < 0$ may exist in vicinity of the BH. For a Schwarzschild BH, $\mathcal{G} = 48M^2/r^6 > 0$, where M is the mass of the BH, and thus $\eta \gtrsim 0$ suffices to create an instability region leading to the growth of the scalar [83]. More generally, when the BH is spinning, $\mathcal{G}$ may change sign around the poles. For $\eta \gtrsim 0$ a similar situation to the spinless case occurs near the equator, whereas for $\eta \lesssim 0$, and large enough dimensionless spin parameter $a \gtrsim 0.5$, a *spin-induced* instability can occur in the region near the poles [84].

As this instability triggers an exponential growth of the scalar in the vicinity of the BH, the nonlinear terms in $f'(\Psi)$ will eventually become as large as the linear term. Spontaneous scalarization for BHs (originally discovered for neutron stars in Damour-Esposito-Farèse theory [85]) in sGB theory occurs when nonlinearities are such that at a later stage the instability is quenched and the system can settle to a stable configuration with nontrivial scalar hair [83,86,87]—as illustrated in Fig. 1; see also Ref. [78] for a review. For the model (9) the transition to the final configuration will depend on the parameter ζ since the nonlinear terms associated to it will be dominant for large $|\Psi|$. A back-of-the-envelope calculation suggests that the end of the tachyonic instability (where the effective mass vanishes) occurs when the scalar reaches a final (maximum) scalar amplitude of order $\Psi \sim \pm\sqrt{-\eta/\zeta}$, for ζ with opposite sign to η. For stability, the value of ζ is further required to satisfy $\eta/\zeta \lesssim -0.8$ [82,88]. The parameter space for such hairy black hole solutions can be characterized in terms of the black hole mass M and corresponding *scalar charge*—see e.g. Ref. [89] for the parameter space in a similar exponential model.

Here we define the scalar charge (per unit mass squared) as

$$q \equiv -\lim_{R\to\infty}\frac{1}{4\pi M^2}\oint_{S_R} dS\,\hat{s}^i\partial_i\Psi, \tag{11}$$

where the integral is taken over a sphere of radius R, and $\hat{s}^i$ is the outward normal to the sphere. This definition of the scalar charge coincides with the usual definition through the scalar falloff at infinity, i.e. $\Psi(r\to\infty) = \Psi_\infty + qM^2/r + \mathcal{O}(r^{-2})$—see e.g. Ref. [89]. Notice also that, for a generic model $f(\Psi)$, the scalar charge does not necessarily correspond to a conserved Noether charge.

As we will see in Sec. III, our basic set up will consist on perturbing GR solutions to obtain such hairy BHs.

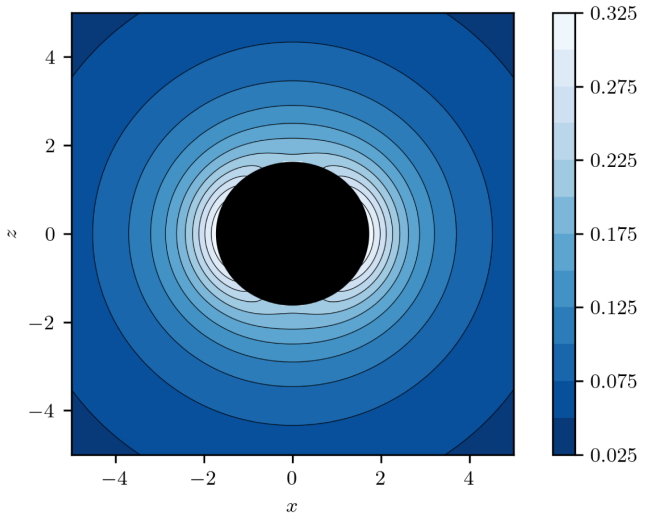

FIG. 1. Scalarized spinning BH. Curvature-induced scalarization for a spinning BH with spin $a = 0.6$ in the $+z$ direction (top) evolved in the decoupling limit [Eq. (8)] for model (9). We have set $\{\ell^2/M^2 = 1, \eta = 6, \zeta = -60\}$. In color, the absolute value of the scalar field Ψ at $t/M = 1000$. See Sec. IV for more details.

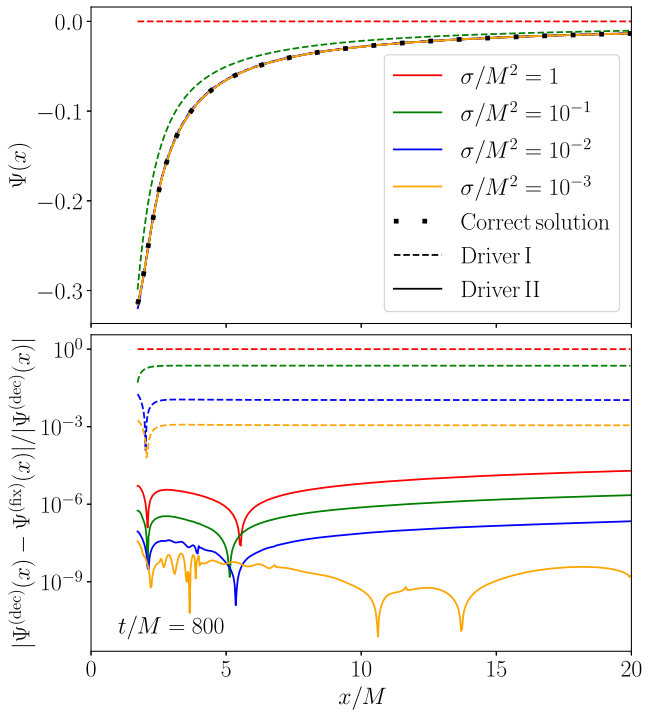

FIG. 2. Scalarized spinning BH (equatorial profile). Top: scalar profile (solid black) for the BH of Fig. 1 along the equatorial $+x$ direction at $t/M = 800$. In colored lines, various approximations with the fixing-the-equations approach. Dashed lines correspond to driver I [Eq. (16)] whereas solid lines correspond to our *new* driver II [Eq. (19)]. We fix $\tau = \sigma/M$. The scalar profiles are plotted starting from the excision sphere, slightly inside the apparent horizon of the BH. Bottom: relative error in the scalar profile with respect to the correct solution given by the decoupling limit [Eq. (8)].

B. Fixing the equations of scalar Gauss-Bonnet gravity

Before using the methods of NR to obtain numerical predictions, further mathematical treatment is often needed to bring the evolution equations into the form of a strongly hyperbolic PDE system—which under appropriate initial conditions can then allow for local well-posedness of the IVP. For GR, this procedure often makes use of auxiliary variables, constraint equations and gauge freedom—some widely used families of formulations include the Z4 and generalized harmonic systems.

For the equations of full sGB theory [Eqs. (3)–(7)] rewriting these equations in such a way is no trivial task. All of the existing approaches (either perturbative [42] or with modified gauges [57,58,61,62]) are valid only at *weak coupling* in ℓ^2, where the corrections with respect to GR are assumed to remain suitably small.

In the fixing-the-equations approach [63], we replace the terms that alter the principal part of the system (the terms with the highest order of derivatives) with new variables subject to *ad hoc driver* equations. The aim is to have the system react in a time scale τ such that it will have the effect of damping (high-frequency) modes ω with $\omega \gtrsim 1/\tau$ which are suspected of leading to instabilities during the evolution. As of yet, there is no unique prescription for the terms to replace nor on the precise form of that the driver equations need to have. In Sec. II D we will use precisely this freedom to devise a driver equation adapted to the problem of recovering stationary solutions.

For the equations of sGB [Eqs. (3) and (4)], we replace the right-hand side of the equations with new variables $\{\Sigma, M_{ab}\}$ to obtain [68]

$$\Box\Psi = \Sigma, \qquad G_{ab} = \kappa T^{(\Psi)}_{ab} + \kappa M_{ab}. \tag{12}$$

In this way, the principal part of Eq. (12) is reduced to that of the simpler Klein-Gordon and Einstein equations, for which the standard methods to rewrite them as strongly hyperbolic systems apply.

To close the system, additional evolution equations that ensure that the auxiliary variables approach their corresponding physical source terms on a specified time scale must be prescribed for $\{\Sigma, M_{ab}\}$. The simplest example for such *driver* equations is [65]

$$\begin{aligned} \tau\partial_t\Sigma &= -(\Sigma - \mathcal{S}), \\ \tau\partial_t M_{ab} &= -(M_{ab} - S_{ab}), \end{aligned} \tag{13}$$

where

$$\mathcal{S} \equiv -\ell^2 f'(\Psi)\mathcal{G}, \qquad \mathcal{S}_{ab} \equiv \ell^2 H_{ab}, \tag{14}$$

and τ is a relaxation timescale (with units of mass) controlling how fast the new variables approach the original source terms. (Notice the parallel of Eq. (13) to exponential decay laws or to constraint damping terms in NR.) In some sense, if the action (1) is thought as an effective field theory, the damping of high frequencies can be interpreted as a way to "soften" the truncation of the theory in a way that allows one to obtain quantitative predictions.

Finally, to compute or replace the second-order time-derivative terms ($\partial_t^2\Psi$ or $\partial_t^2 g_{ab}$) remaining in $\{\mathcal{S}, \mathcal{S}_{ab}\}$, additional techniques may be required, such as *order reduction* [65], where the leading order equations of motion (in ℓ^2) would be used to reduce the order of second-order time-derivative terms.

Although Eq. (13) may be the simplest form of driver equations, in practice, they may not be the most convenient in an actual numerical implementation since they result in standing modes for $\{\Sigma, M_{ab}\}$, instead of propagating modes. Indeed, in Ref. [68], numerical relativity simulations of the fully coupled system (12) have been performed in spherical symmetry using a driver equation with wavelike properties. We will consider other alternatives for these driver equations in Sec. II D.

C. Case study: Fixing the decoupling limit of scalar Gauss Bonnet

As remarked in Sec. I, in this paper, we take our first steps towards an implementation in full 3-dimensional space. Since such an undertaking is far more complex than that of Ref. [68], for simplicity, we begin by studying the scalar dynamics of system (12), i.e. we will "fix" the decoupling limit of scalar Gauss-Bonnet theory. To be more precise, we will evolve

$$\Box\Psi = \Sigma, \qquad R_{ab} = 0, \tag{15}$$

where the auxiliary variable Σ is subject to a driver equation to be specified below.

In this particular case, the original decoupling limit equations [Eq. (3) and $R_{ab} = 0$] can be cast as a strongly hyperbolic system and can be readily evolved without fixing. Therefore, this set up will be useful as an exercise to test the numerical implementation of the system as well as to evaluate whether it can accurately describe the dynamics of the scalar and the final stationary solutions. Indeed, we can directly compare with the solutions of the unmodified theory, which are, in some sense the "exact" solution which one would like to recover with the fixing-the-equations approach.

D. Advanced drivers and recovery of stationary solutions

In this section we consider more complex choices for driver equations for scalar variables. We will begin by considering a driver equation first presented in Ref. [69] (with some slight modifications[1])

$$\sigma(\partial_t - \beta^i\partial_i)^2\Sigma + \tau(\partial_t - \beta^i\partial_i)\Sigma = -(\Sigma - \mathcal{S}), \tag{16}$$

where α is the lapse, $\beta^i = \gamma^{ij}\beta_j$ is the shift, and γ_{ij} is the spatial metric (with inverse γ^{ij}) in the $(3+1)$ decomposition of the spacetime metric

$$\begin{aligned} ds^2 &= g_{ab}dx^a dx^b \\ &= -\alpha^2\, dt^2 + \gamma_{ij}(\beta^i dt + dx^i)(\beta^j dt + dx^j), \end{aligned} \tag{17}$$

and also where $\mathcal{S} \equiv -\ell^2 f'(\Psi)\mathcal{G}$ and $\{\sigma, \tau\}$ are dimensionful non-negative parameters (with dimensions $[\text{mass}]^2$ and [mass], respectively) that will control the relaxation time scale(s) of Σ towards the desired value given by $\mathcal{S}$. In the following, we will refer to Eq. (16) as *driver I*. Just as Eq. (13) is reminiscent of exponential decay laws, by looking at the time-derivative terms, Eq. (16) is reminiscent of a forced damped harmonic oscillator, $\ddot{x}(t) + 2\zeta_d\omega_0\dot{x}(t) + \omega_0^2 x(t) = \mathcal{F}$, where $\omega_0 \equiv 1/\sqrt{\sigma}$ is the oscillator frequency, $\zeta_d \equiv \tau/(2\sqrt{\sigma})$ is the damping parameter, and the source $\mathcal{S}$ enters as a forcing term $\mathcal{F} \equiv \mathcal{S}/\sigma$. Moreover, it is clear that the advective operators $(\partial_t - \beta^i\partial_i)$ entering driver I are such that the propagating modes will move in the opposite direction of β^i. For BH spacetimes (depending on the specific gauge) these modes can become ingoing (into the hole) near apparent horizons, thus allowing inaccuracies in the tracking of the source term to propagate outside of the region of interest.

While driver I has many desirable properties, one issue associated with it (already pointed out in Ref. [69]), as well as with related wavelike drivers of the form (such as the one of Ref. [68])

$$-\sigma\Box\Sigma + \tau(\partial_t - \beta^i\partial_i)\Sigma = -(\Sigma - \mathcal{S}), \tag{18}$$

is that stationary solutions are not recovered exactly. To see this, consider a stationary situation, with respect to the coordinate t associated with an approximate Killing vector $\chi = \partial_t$. Assuming that all fields have become time independent $\Sigma(t, x^i) = \Sigma(x^i)$, we can set to zero all the time derivatives in driver I. The resulting equation, $\sigma(\beta^i\partial_i)^2\Sigma - \tau\beta^i\partial_i\Sigma = -(\Sigma - \mathcal{S})$, still contains spatial derivative operators. If $\mathcal{S}$ is spatially dependent (as for any non-trivial solution), $\Sigma = \mathcal{S}$ cannot be a solution, and driver I will not reproduce the correct answer. Nevertheless, one would expect that these errors would decrease as $\{\sigma, \tau\}$ are decreased—or as the relaxation time scales associated

[1]The precise difference between the driver equation here and that in Ref. [69] lies in the terms with the lowest derivatives (e.g. terms proportional to first derivatives of the lapse and shift), as well as multiplicative factors of the lapse.

to these parameters are decreased. In Sec. IV we will show with examples that this indeed seems to be the case.

To address this issue, we propose a *new* driver given by

$$\sigma(\partial_t-\beta^i\partial_i)(\partial_t+v^i\partial_i)\Sigma+\tau(\partial_t+v^i\partial_i)\Sigma=-(\Sigma-\mathcal{S}). \quad (19)$$

In the following, we will refer to this equation as *driver II*. For a BH in uniform motion, we identify v^i as the velocity of the BH as obtained from the trajectory of the center of the apparent horizon. The *new* driver equation has now the desired limit to recover stationary solutions, which can be seen as follows: proceeding as before, for a BH with zero linear momentum ($v^i=0$), setting the time derivatives to zero gives indeed $\Sigma=\mathcal{S}$. Whereas for a BH with linear momentum, the same should hold since one can identify $D_t\equiv\partial_t+v^i\partial_i$ as the *convective* time derivative. In Sec. IV, we will show that indeed Eq. (19) gives an improved recovery over Eq. (16).

III. METHODOLOGY

A. First-order reduction

All of the component subsystems of Eqs. (8) and (15) are decoupled and can be written individually in first-order symmetric hyperbolic form

$$\partial_t\boldsymbol{u}+\mathbb{A}^i\partial_i\boldsymbol{u}=\boldsymbol{\mathcal{S}}(\boldsymbol{u}), \quad (20)$$

where $\boldsymbol{u}$ are first-order variables, $\mathbb{A}=\mathbb{A}(\boldsymbol{u})$ is a square symmetric matrix that may depend on $\boldsymbol{u}$ (but not its derivatives), and $\boldsymbol{\mathcal{S}}(\boldsymbol{u})$ is a source term.

The principal part of the scalar equation for Ψ is that of Klein-Gordon equation. Therefore, we introduce first-order variables

$$\boldsymbol{u}\equiv\{\Psi,\Phi_i^{(\Psi)}\equiv\partial_i\Psi,\Pi^{(\Psi)}\equiv-n^c\partial_c\Psi\}, \quad (21)$$

where $n_c\equiv-\alpha\delta_c^0$ is the unit normal to the hypersurface, and rewrite the scalar equation as

$$\begin{aligned}\partial_t\Psi-(1+\gamma_1^{(\Psi)})\beta^i\partial_i\Psi&\simeq0,\\ \partial_t\Pi^{(\Psi)}-\beta^k\partial_k\Pi^{(\Psi)}+\alpha\gamma^{ik}\partial_i\Phi_k^{(\Psi)}-\gamma_1^{(\Psi)}\gamma_2^{(\Psi)}\beta^i\partial_i\Psi&\simeq0,\\ \partial_t\Phi_i^{(\Psi)}-\beta^k\partial_k\Phi_i^{(\Psi)}+\alpha\partial_i\Pi^{(\Psi)}-\gamma_2^{(\Psi)}\alpha\partial_i\Psi&\simeq0.\end{aligned} \quad (22)$$

Here, $\gamma_{1,2}^{(\Psi)}$ are constraint damping parameters and the $\simeq0$ notation indicates that only the principal part terms are displayed—see Ref. [90] for the full expressions.

The Einstein field equations in the generalized harmonic gauge have a principal part of the form $g^{cd}\partial_c\partial_d g_{ab}\simeq0$, and can therefore be written in a first-order form analogous to that of the Klein-Gordon equation. We refer to Lindblom *et al.* [91] for the full first-order equations employed here, where the first-order variables are given by

$$\boldsymbol{u}\equiv\{g_{ab},\Phi_{iab}\equiv\partial_i g_{ab},\Pi_{ab}\equiv-n^c\partial_c g_{ab}\}. \quad (23)$$

The first-order form for the driver sector depends on the particular driver used. For Eq. (16) it reads

$$\begin{aligned}(\partial_t-\beta^i\partial_i)\Sigma&=-\alpha\Pi^{(\Sigma)},\\ \sigma(\partial_t-\beta^i\partial_i)\Pi^{(\Sigma)}&=-\alpha^2\tau\Pi^{(\Sigma)}+\alpha(\Sigma-\mathcal{S}),\end{aligned} \quad (24)$$

whereas for Eq. (19), it is given by

$$\begin{aligned}(\partial_t+v^i\partial_i)\Sigma&=-\alpha\Pi^{(\Sigma)},\\ \sigma(\partial_t-\beta^i\partial_i)\Pi^{(\Sigma)}&=-\alpha^2\tau\Pi^{(\Sigma)}+\alpha(\Sigma-\mathcal{S}).\end{aligned} \quad (25)$$

Both systems depend on the first-order variables $\boldsymbol{u}\equiv\{\Sigma,\Pi^{(\Sigma)}\}$, where $\Pi^{(\Sigma)}$ is defined by the first equation of each system. Notice that we do not need to introduce a first-order variable $\Phi_i^{(\Sigma)}$ for $\partial_i\Sigma$.

Finally, the Gauss-Bonnet scalar (in vacuum $R_{ab}\equiv0$) appearing in the sources of the scalar equations for $\{\Psi,\Sigma\}$ is computed in practice as

$$\mathcal{G}=C_{abcd}C^{abcd}=8(E_{ij}E^{ij}-B_{ij}B^{ij}), \quad (26)$$

where $E_{ij}\equiv n^a n^b C_{aibj}$ and $B_{ij}\equiv-n^a n^b\,{}^*C_{aibj}$ are the electric and magnetic parts (respectively) of the Weyl tensor C_{abcd}, with left dual ${}^*C_{abcd}\equiv\frac{1}{2}\epsilon_{abef}C^{ef}{}_{cd}$–their full expressions in terms of $(3+1)$-decomposition quantities are given in Eqs. (B7) and (B8) of Ref. [42].

B. Evolution code

We implement systems (8) and (15) in SpECTRE [64], an open-source code based on task-based parallelism.

The full system is discretized following a discontinuous Galerkin (DG) scheme employing a numerical upwind flux. Evolution in time is carried out by means of a fourth-order Adams-Bashforth time stepper with local adaptive time-stepping [92], and we apply a weak exponential filter on all evolved fields at each time step. The spatial domain is illustrated in Fig. 3 and consists of a series of concentric spherical shells. The outer boundary is located at $R/M=500$, while the inner boundary conforms to the shape of the apparent horizon. Each shell is further decomposed into elements isomorphic to unit cubes, endowed with a tensor product of Legendre polynomials.

The implementation of the scalar sector with a Klein-Gordon equation has been recently been described in detail in Ref. [90]. In particular, we impose constraint-preserving spherical-radiation boundary conditions [93] on the scalar field Ψ. The constraint damping parameters $\{\gamma_1^{(\Psi)},\gamma_2^{(\Psi)}\}$ are modulated by Gaussian profiles

$$\gamma_J(\boldsymbol{x})\equiv C_J+A_J\exp\left(-\frac{|\boldsymbol{x}-\boldsymbol{x}_{c,J}|^2}{2w_J^2}\right), \quad (27)$$

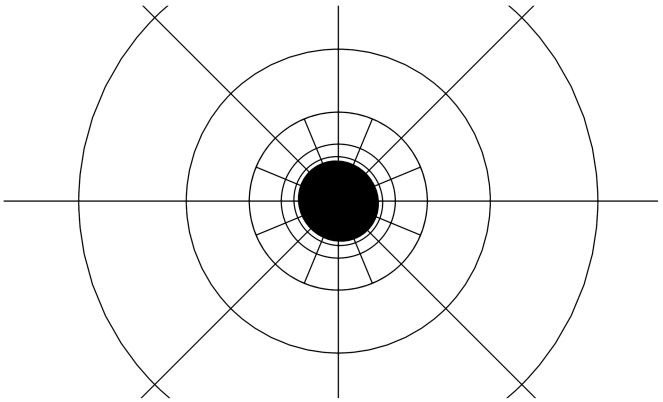

FIG. 3. Spatial domain and apparent horizon. Domain decomposition for a black hole with (dimensionless) spin $\boldsymbol{\chi} = 0.6\hat{\boldsymbol{s}}$, where $\hat{\boldsymbol{s}} = (1/\sqrt{2}, 0, 1/\sqrt{2})$, in the xz plane depicted above. The black lines correspond to discontinuous Galerkin element boundaries. The solid black region is delimited by the apparent horizon of the BH.

centered around the black hole $\boldsymbol{x}_{c,J} = \boldsymbol{x}_{\rm BH}$. We set $\gamma_1^{(\Psi)} \equiv 0$ and specify $\gamma_2^{(\Psi)}$ through the parameters $\{A = 6, w = 11M, C = 10^{-3}\}$.

For the metric sector, the full details of the numerical implementation will be presented in a specialized publication elsewhere [94], and we only broadly summarize the most relevant aspects here. The evolution system for the metric variables in the GH gauge is given in Ref. [91] and is implemented in a dual-frame formulation [95]. The constraint-damping parameters $\{\gamma_0, \gamma_1, \gamma_2\}$ follow a spatial distribution of the form (27). We choose $\gamma_1 \equiv -1$ and $\{A = 3, w/M = 11, C = 10^{-3}\}$ for γ_0 and γ_2. The gauge functions H_a in the GH system are evolved in damped harmonic (DH) gauge [96–98]. A portion of the domain inside the apparent horizon is excised and no boundary conditions are imposed at the excision sphere—we monitor, however, that at that boundary all characteristic fields have velocities flowing out of the computational domain, so that no boundary condition is required for the evolution to remain well posed. Finally, constraint-preserving Bjorhus boundary conditions [91,99] are imposed at the outer boundary.

For the scalar driver part, the implementation is similar to that of the scalar field. We monitor that the characteristic velocities are flowing out of the computational domain at the excision sphere and impose zero Dirichlet boundary conditions (i.e. $\Sigma|_{\rm out} \equiv 0$) at the outer boundary of the spatial domain. Further, we allow for a Gaussian spatial dependence of the form (27) for the parameters $\{\sigma, \tau\}$ introduced in the driver equation for Σ. We choose $\{w/M = 150, C = 1\}$ for σ, $\{w/M = 150, C = 10^{-4}\}$ for τ and vary the amplitude A for both parameters. For simplicity, when we quote values of $\{\sigma, \tau\}$, we refer to their values at the center of the Gaussian profile.

C. Initial data

We choose as initial data a *hairless* Kerr black hole subject to an initial scalar perturbation on Ψ. As remarked in Sec. II, this solution is unstable and is expected to migrate during the evolution to a stable *hairy* black hole.

For the metric variables, we choose Kerr-Schild initial data (with $M = 1$), in Cartesian coordinates $\boldsymbol{x} = (x, y, z)$,

$$g_{ab} = \eta_{ab} + \mathcal{H} l_a l_b. \tag{28}$$

Here $\eta_{ab} = \mathrm{diag}(-1, 1, 1, 1)$ is the Minkowski metric, and the scalar function $\mathcal{H}$ and one-form l_a (which satisfies $l^c \partial_c l_a = l^c \nabla_c l_a = 0$) are given by

$$\mathcal{H} \equiv \frac{M\rho^3}{\rho^4 + a^2 z^2}, \tag{29}$$

$$l_a \equiv \left(1, \frac{\rho x + a y}{\rho^2 + a^2}, \frac{\rho y - a x}{\rho^2 + a^2}, \frac{z}{\rho}\right), \tag{30}$$

where the spin direction is along the $+z$ direction, ρ is implicitly defined through $\rho^2(x^2 + y^2) + (\rho^2 + a^2)z^2 = \rho^2(\rho^2 + a^2)$, and a is the dimensionless spin parameter of the BH.

For the case of a BH with linear momentum, we obtain a boosted Kerr-Schild solution by applying the appropriate Lorentz boost to the coordinates x^a and l_a.

To induce the scalarization of the BH, we prescribe a scalar perturbation of the form [100]

$$\begin{aligned} \Psi(r)|_{t=0} &= \Phi_i^{(\Psi)}(r)|_{t=0} \equiv 0, \\ \Pi^{(\Psi)}(r)|_{t=0} &\equiv \mathcal{A}\mathrm{Re}[e^{-(r-r_0)^2/w^2} Y_{lm}(\theta, \phi)], \end{aligned} \tag{31}$$

where $Y_{lm}(\theta, \phi)$ are spherical harmonics and $\{\mathcal{A}, w, r_0\}$ are the amplitude, width and radius of the scalar profile.

For the quartic model (9), this initial data for Ψ implies that initially the scalar source vanishes, i.e. $\mathcal{S}|_{t=0} \equiv -\ell^2 f'(\Psi)\mathcal{G}_{\rm GB} = 0$. Therefore, we prescribe zero initial conditions for the scalar driver, i.e.

$$\Sigma|_{t=0} = \Pi^{(\Sigma)}|_{t=0} \equiv 0. \tag{32}$$

D. Comparison strategy and diagnostics

For each of the examples in Sec. IV we evolve three systems of equations with the same initial data. These are

(1) The (unmodified) decoupling limit equations (8). We label these solutions $\Psi^{(\rm dec)}$.
(2) The fixed decoupling limit equations (15) with Σ evolved using driver I [Eq. (16)]. We label these solutions $\Psi^{(\rm fix,I)}$.
(3) The fixed decoupling limit equations (15) with driver II [Eq. (19)]. We label these solutions $\Psi^{(\rm fix,II)}$.

We compare the scalar field volume configurations across the different systems (decoupling limit against the fixed versions of the decoupling limit) by computing a relative *accuracy estimates* of the form

$$\mathcal{E}[Q] \equiv \frac{\|Q^{(\mathrm{dec})} - Q^{(\mathrm{fix})}\|}{\|Q^{(\mathrm{dec})}\| + \epsilon}, \tag{33}$$

where Q is the desired quantity to compare, $\|\cdot\|$ is a suitable norm and ϵ is a small number.

The accuracy estimate for the scalar field profile along a direction, for instance, in the x direction, is given by

$$\mathcal{E}[\Psi(x)](t) \equiv \frac{|\Psi^{(\mathrm{dec})}(x) - \Psi^{(\mathrm{fix})}(x)|}{|\Psi^{(\mathrm{dec})}(x)| + \epsilon}. \tag{34}$$

When we compare the across the whole spatial domain we can define (see Refs. [65,67] for similar measures)

$$\mathcal{E}[\Psi](t) \equiv \frac{\|\Psi^{(\mathrm{dec})} - \Psi^{(\mathrm{fix})}\|_2}{\|\Psi^{(\mathrm{dec})}\|_2 + \epsilon}, \tag{35}$$

$\|\cdot\|_2$ is the L_2 norm with respect to the grid points $\{x_i\}$,

$$\|y\|_2^2 \equiv \frac{1}{N}\sum_{i=1}^{N} y(t, x_i)^2, \tag{36}$$

with N being the number of grid points.

We monitor the accuracy of the auxiliary field tracking the original value of the source term with (see Refs. [67,69] for similar measures)

$$\mathcal{E}[\mathcal{S}](t) \equiv \frac{\|\Sigma - \mathcal{S}\|_2}{\|\mathcal{S}\|_2 + \epsilon}. \tag{37}$$

Finally, we compute an accuracy estimate error for the scalar waveform, which is an example of an observable quantity. We define the accuracy estimate for the rms waveform $\sqrt{\langle\Psi^2\rangle}$ by

$$\mathcal{E}\left[\sqrt{\langle\Psi^2\rangle}\right](t; R) \equiv \frac{\left|\sqrt{\langle\Psi^2\rangle^{(\mathrm{dec})}} - \sqrt{\langle\Psi^2\rangle^{(\mathrm{fix})}}\right|}{\left|\sqrt{\langle\Psi^2\rangle^{(\mathrm{dec})}}\right| + \epsilon}, \tag{38}$$

where $\sqrt{\langle\Psi^2\rangle}$ is extracted at 6 equally spaced spheres in the range $R/M \in [50, 100]$ and for which the sphere average of the square of the scalar amplitude is computed as

$$\langle\Psi^2\rangle \equiv \frac{1}{4\pi R^2}\oint_{S_R} dS\Psi^2. \tag{39}$$

1. Constraints

We keep track of the first-order constraints for the scalar field to monitor the evolution. These are given by

$$\mathcal{C}_i^{(\Psi)} \equiv \partial_i\Psi - \Phi_i, \qquad \mathcal{C}_{ij}^{(\Psi)} \equiv \partial_i\Phi_j - \partial_j\Phi_i. \tag{40}$$

For the metric we keep track of the following constraints:

$$\begin{aligned} \mathcal{C}_a &\equiv H_a + \Gamma_a, & \mathcal{C}_{ia} &\simeq \partial_i C_a, \\ \mathcal{C}_{iab} &\equiv \partial_i g_{ab} - \Phi_{iab}, & \mathcal{F}_a &\simeq n^c\partial_c\mathcal{C}_a, \end{aligned} \tag{41}$$

where $\mathcal{C}_{ia}$ and $\mathcal{F}_a$ are given in full in Eqs. (43) and (44) of Ref. [91]. Here, $\Gamma_a \equiv g_{ab}g^{cd}\Gamma^b_{cd}$ is a contraction of the 4-dimensional Christoffel symbol Γ^a_{bc}. Given the symmetric hyperbolic nature of the metric evolution equations, a symmetrizer can be constructed, and thus these constraints can be further condensed in a constraint energy $\mathcal{E}_c$—given in Eq. (53) of Ref. [91].

IV. RESULTS

In the following, we illustrate with various examples the ability of our implementation of the fixing-the-equations approach to reproduce the scalar dynamics of the decoupling limit of sGB theory.

A. Spinning black holes

We start with an initially hairless Kerr BH with dimensionless spin parameter $a = 0.6$ and with zero linear momentum. We set the coupling parameters to $\{\eta = 6, \zeta = -60\}$ and induce spontaneous scalarization by perturbing the BH with an initial scalar profile [Eq. (31)] with parameters $\{\mathcal{A} = 10^{-5}, w/M = 5, r_0/M = 30, (l, m) = (0, 0)\}$. In Fig. 1 we show the final stationary hairy solution in the decoupling limit (the correct solution we are seeking to recover) against which we will compare the results obtained with different fixing-the-equations schemes. We then evolve the same set of initial data in the fixing-the-equations approach for both driver I and for our new driver II to obtain stationary solutions. Since the strongest dependence is on the σ parameter, for simplicity, we fix $\tau = \sigma/M$ and vary only σ. We choose values of $\sigma/M^2 \leq 1$ such that the driver equations are in the underdamped regime $\zeta_d < 1$ in the parallel made in Sec. II D with the damped harmonic oscillator.

The most straightforward comparison of the solutions is that of the scalar profile along a radial direction at late times. In the top panel of Fig. 2 we plot the scalar field along the x axis (in the equatorial plane) for the exact solution (solid black) and for the different *fixing-the-equations* approximations (colored lines). In the bottom panel, we plot the accuracy estimate for the radial profile with respect to the exact solution. We observe that as σ is decreased, the solutions obtained with both driver I and II approach the desired solution. For instance, for the largest choice of parameters, $\sigma/M^2 = 1$, the solution with driver I (dashed red) completely fails to reproduce the scalarized solution, giving a vanishing scalar profile everywhere.

As sigma is decreased to $\sigma/M^2 = 10^{-1}$ (dashed green), the solution obtained with this driver is qualitatively similar in shape to the exact solution, but underestimated in magnitude by about 20%. For smaller values of σ, the agreement with the exact solution is close enough that it is no longer apparent in the top panel, and they yield an accuracy estimate of $\lesssim 1\%$. This is to be expected since $\sqrt{\sigma}$ is a timescale (length scale) that controls how closely the driver variable Σ is tracking the intended source term $\mathcal{S}$. Nevertheless, it is apparent that driver II (solid lines) reproduces the correct solution far more accurately than driver I. Even for the largest parameters $\sigma/M^2 = 1$, the agreement with the stationary solution is better than the best solution obtained with driver I.

Having focused on late times in the previous paragraph, we now turn to analyzing the tracking in time throughout all of the scalarization event. In our implementation of the fixing-the-equations approach, Σ acts as the source term of the scalar field Ψ. To correctly capture the physics of the system, it needs to accurately track the original value of the source term $\mathcal{S} \equiv -\ell^2 f'(\Psi)\mathcal{G}$. In order to evaluate how well Σ is tracking $\mathcal{S}$, in Fig. 4 we compute the accuracy estimate for the scalar source term [Eq. (37)] as a function of time. Since $\mathcal{S}$ is initially vanishing, the accuracy estimate is largest at the beginning of the simulation. Moreover, the source term is proportional to $\mathcal{G}$, which scales as $1/r^6$. Therefore, it remains significantly small during the immediate evolution. We ignore the very early peak since we consider the relative accuracy estimate to not be meaningful there. A second peak at $t/M \simeq 100$ corresponds to the time when the tachyonic instability in the scalar is active and the scalar hair is growing at the fastest rate. At late times, as the scalar settles into a stationary situation, the estimate tends to an (almost) constant value. As before, the accuracy estimate decreases as σ is decreased. Whereas driver I is limited at late times to approach $\mathcal{S}$ exactly by nonvanishing spatial derivative terms, our new driver II was designed to avoid this issue—recall the discussion in Sec II D. Therefore, the improved behavior of our new driver II (in solid lines) is apparent throughout the entire evolution: the accuracy estimate of $\mathcal{S}$ is generally smaller, decreases faster and achieves much lower values at late times. We have observed similar behavior when we decrease the value of τ with respect to σ.

Since Ψ and Σ are related through a differential equation, the tracking the source term is an indirect comparison of the dynamics of the scalar field. A more direct comparison however is to compare the full 3-dimensional scalar configuration of the fixing-the-equations approximations against that of the correct solution. In Fig. 5, we plot the accuracy estimate in time of the spatial scalar profiles with respect to the reference, which confirms that the tracking behavior of the source term Σ observed before directly translates into a good tracking of the dynamics of Ψ. As

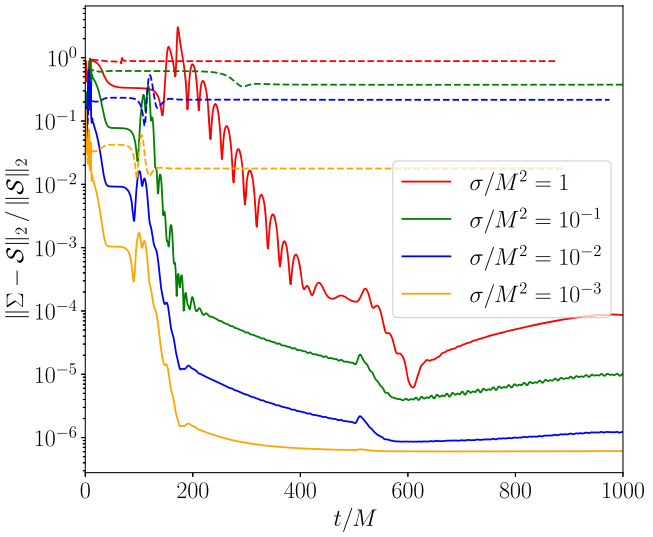

FIG. 4. σ dependence for the accuracy estimate of the scalar source tracking (spinning). Accuracy estimate for the scalar source (dashed lines) [Eq. (37)] for driver I [Eq. (16)] as a function of time and for different values of sigma and where we fix $\tau = \sigma/M$. Also in the plot, the same accuracy estimate (solid lines) for the driver II [Eq. (19)].

opposed to the tracking estimate in Fig. 4, this estimate is meaningful throughout the simulation.

Finally, we turn to comparing an observable quantity: the scalar waveform. In the top panel of Fig. 6, we plot the rms scalar waveform extracted at $R/M = 100$ as well as the waveform in the exact solution. For completeness, we also

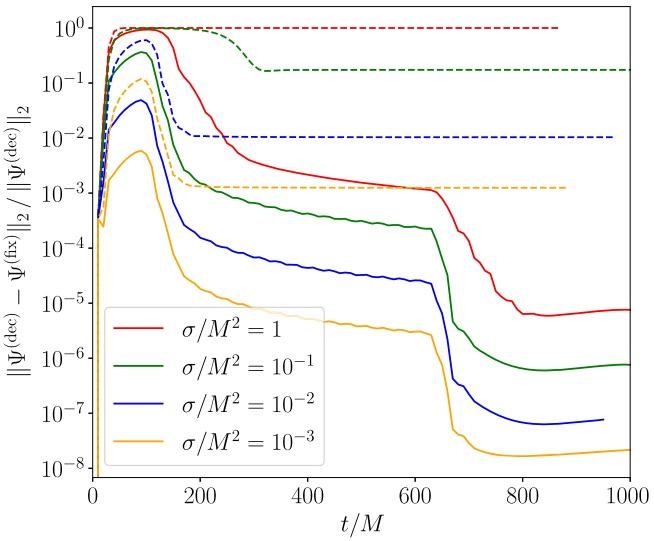

FIG. 5. σ dependence for the accuracy estimate in scalar field slices (spinning). Accuracy estimate for the scalar field 3-dimensional slices (dashed lines) [Eq. (35)] for driver I [Eq. (16)] as a function of time and for different values of sigma and where we fix $\tau = \sigma/M$. Also in the plot, the same accuracy estimate (solid lines) for the driver II [Eq. (19)].

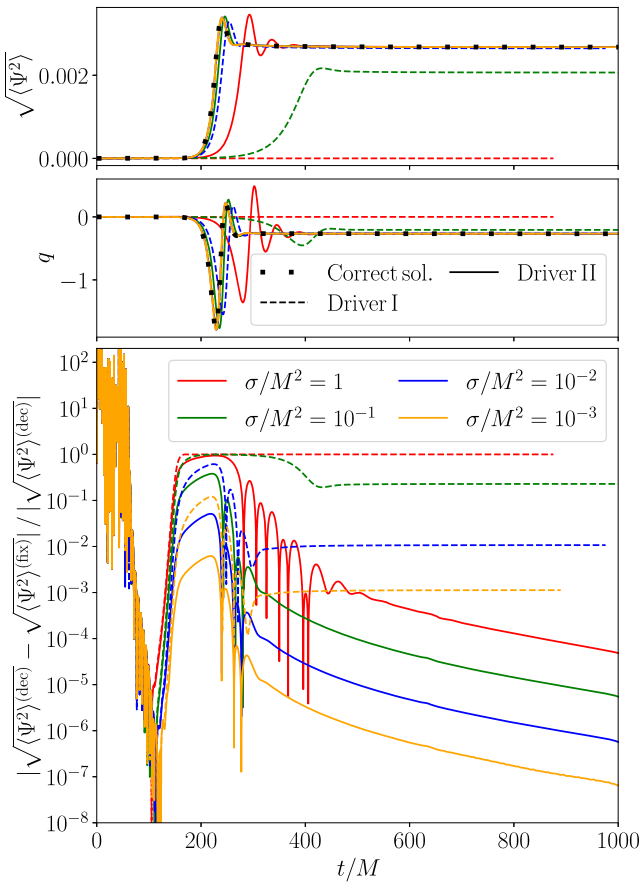

FIG. 6. σ dependence for the accuracy estimate of the scalar wave (spinning). Top panel: rms scalar wave extracted at $R/M = 100$. We compare the signal between the correct solution (black dots) [evolved with Eq. (8)], the signal obtained for driver I (dashed lines) [Eq. (16)] and the signal obtained for driver II (solid lines) [Eq. (19)]. Middle panel: corresponding scalar charge (per unit mass squared) [Eq. (11)] extracted at the same finite radius and for which the correct solution asymptotes to $q \simeq -0.267$. Bottom panel: the accuracy estimate for the rms scalar wave [Eq. (38)] of the top panel shows that driver II outperforms driver I also in the dynamics.

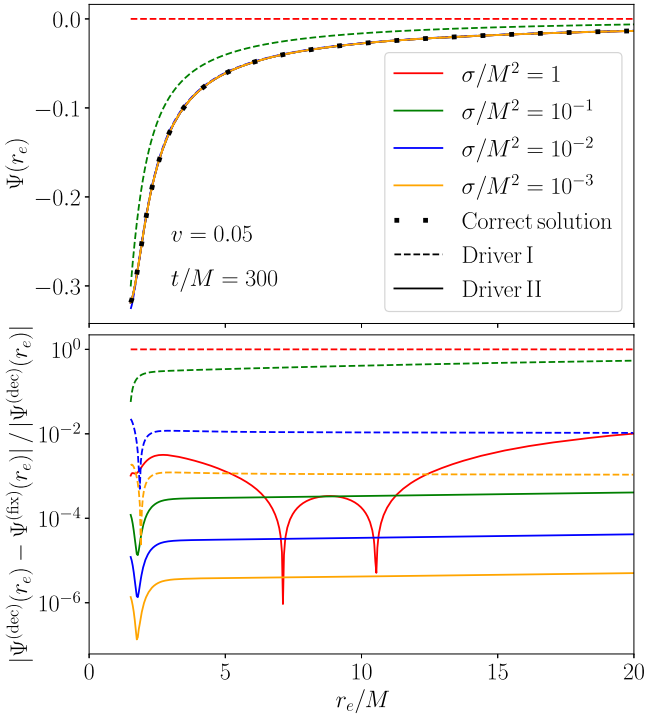

FIG. 7. Boosted scalarized spinning BH (equatorial profile). In this example the BH is spinning $\boldsymbol{\chi} = 0.6\hat{\boldsymbol{s}}$, along the direction $\hat{\boldsymbol{s}} = (1/\sqrt{2}, 0, 1/\sqrt{2})$ and is also boosted with velocity $\boldsymbol{v} = (0.05, 0, 0)$. Top: scalar profile (solid black) for the BH of Fig. 1 along the equatorial direction r_e (at $-45°$ in the xz-plane) at $t/M = 300$. We show the scalar profile (dashed lines) corresponding to driver I [Eq. (16)] as well as the scalar profile (solid lines) corresponding to our *new* driver II [Eq. (19)]. We fix $\tau = \sigma/M$. The scalar profiles are plotted starting from the excision sphere, slightly inside the apparent horizon of the BH. Bottom: relative error in the scalar profile with respect to the correct solution given by the decoupling limit [Eq. (8)].

show in the middle panel the corresponding finite-radius approximation of the scalar charge (per unit mass squared) [cf. Eq. (11)], which reaches an asymptotic value of $q \simeq -0.267$. In the bottom panel, the accuracy estimate for the scalar waveform against the correct solution is shown. At early times, the seemingly large accuracy estimate is due to the scalar field being almost zero at the location of the extraction sphere—and as before, this part of the estimate should be disregarded. The scalar field acquires nonzero values (and the estimate quickly decreases) as the outgoing initial perturbation and the scalarization front reach the extraction sphere. In line with the previous discussion, the scalar wave is better tracked with the new driver II (solid lines). For instance, the accuracy estimate for the best case of driver II (orange solid lines) reaches $< 10^{-2}$ at the peak, and is as low as $\lesssim 10^{-7}$ towards the end the evolution. In comparison, the accuracy in the estimate for the corresponding best case for driver I (orange dashed lines) saturates at $\sim 10^{-3}$ after a peak of $\sim 10\%$ in accuracy.

B. Boosted black holes

We now study the case of boosted BH as a test of the applicability of our drivers to the early inspiral phase in BBH system. In addition, this configuration will also test terms proportional to the BH velocity in the convective derivative on which our new driver II is based. We choose an initial boost velocity $\boldsymbol{v} = (0.05, 0, 0)$ and spin unaligned with the direction of motion given by $\boldsymbol{\chi} = 0.6\hat{\boldsymbol{s}}$, along the direction $\hat{\boldsymbol{s}} = (1/\sqrt{2}, 0, 1/\sqrt{2})$—illustrated in Fig. 3. We use the same set of coupling parameters and initial scalar perturbation parameters as in the previous example.

In Fig. 7 we show the scalar profiles along the equator (which in this case is not aligned with the x axis), and in Fig. 8 we plot the scalar waveform and corresponding accuracy estimate for this case. Qualitatively similar

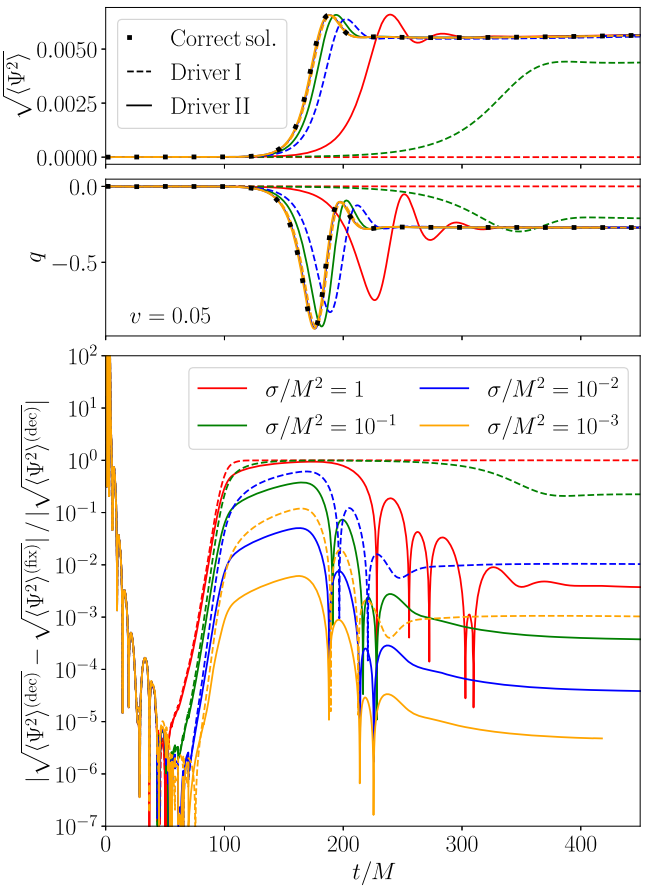

FIG. 8. σ dependence for the accuracy estimate of the scalar wave (boosted BH). Top panel: rms scalar wave extracted at at $R/M = 50$. We compare the signal between the correct solution (black dots) [evolved with Eq. (8)], the signal obtained for driver I (dashed lines) [Eq. (16)] and the signal obtained for driver II (solid lines) [Eq. (19)]. Middle panel: corresponding scalar charge (per unit mass squared) [Eq. (11)] extracted at the same finite radius. and for which the correct solution asymptotes to $q \simeq -0.273$. Bottom panel: the accuracy estimate for the rms scalar wave [Eq. (38)] of the top panel shows that driver II outperforms driver I also in the dynamics.

behavior is seen as in the previous example. Namely, that for both drivers the accuracy improves as σ/M^2 is decreased and that for a given value of σ/M^2 our new driver II improves the accuracy of the scalar equatorial profile and scalar wave by several orders of magnitude compared to the same case evolved with driver I.

There are two noticeable differences with respect to the vanishing BH velocity case. First, the accuracy estimates corresponding to driver II for the equatorial profile and for the scalar wave are larger. Nevertheless, they remain clearly well below the estimate for driver I. Second, the length of the simulations is shorter than in the previous case. In that regard, our simulations currently are limited for larger speeds and longer later times due to an imperfect alignment of the excision sphere with respect to the moving apparent horizon of the BH. Further improvements in automatic control systems are underway to dynamically adjust the location and shape of the excision sphere. This will allow us to control this source of error and to extend these simulations to $v \gtrsim 0.05$ and $t/M \sim \mathcal{O}(10^3)$.

V. CONCLUSION

In this paper, we have reported on recent progress in implementing the fixing-the-equations approach [63] in the numerical relativity code SpECTRE [64] with the aim of obtaining quantitative predictions from BBH coalescence in scalar Gauss-Bonnet theory. In this scheme, the equations of motion are modified by introducing additional variables that replace the correction terms to the GR principal part that can lead to unstable solutions. The evolution of these new variables is controlled by *ad hoc* evolution equations that drive their values to those of the original terms within a certain time scale, effectively damping the high-frequency modes that lead to instabilities in the original equations. In its current stage, our code is able to evolve the scalar, metric and the scalar part of the driver systems in full 3-dimensional space using a discontinuous Galerkin scheme.

Since the driver equations in the fixing-the-equations approach are not uniquely prescribed, another focus of this paper has been to identify effective driver equations that are able to accurately describe the stationary solutions of the theory. Restricting to the decoupling limit of the theory (where we have neglected the back reaction of the scalar field on the metric), we were able to evolve both the original theory and the corresponding fixed theory, and thus evaluate the accuracy of the stationary solutions obtained with different driver equations. By studying different examples of isolated BH that undergo spontaneous scalarization we have confirmed that, both in the stationary case as well as during the scalar dynamics of the scalarization event, one can recover the solutions of the original theory with increasing accuracy by tightening the time scales entering the driver equations.

Moreover, we have presented a new driver equation with an improved stationary limit and have shown that it performs remarkably well in recovering the solutions of the original theory in full 3-dimensional space without symmetries, in comparison with similar drivers in the literature [68,69]. While our tests are encouraging for low BH speeds, further testing at higher speeds would be ideal to confirm that the improved behavior persists in more challenging situations. We leave this for future work as this requires improved control systems to adjust the location of the excision sphere inside the BH.

The results presented here will inform the next stages of our program to simulate BBH systems in the fixing-the-equations approach. From our experience, we have observed that there is a trade-off between increasing accuracy and computational resources. As we have shown

here, by decreasing the time scales in the driver equations, one can obtain more accurate solutions. This comes at the cost of a smaller (minimum) time step required for the evolution—mainly because the driver equation becomes increasingly stiff. By allowing for greater accuracy with larger values of the fixing time scales, we anticipate that the new scalar driver equation presented here (and their required tensorial generalizations needed to handle the back-reaction of the scalar field) will have a beneficial effect in the computational resources needed to evolve such systems, at least during the inspiral stage.

ACKNOWLEDGMENTS

We would like to thank Enrico Barausse, Miguel Bezares, Ramiro Cayuso, Alexandru Dima, Nicola Franchini, Aaron Held, Aron D. Kovacs, Luis Lehner and Peter J. Nee for useful discussions about the fixing-the-equations approach. Computations were performed on the Urania and Raven HPC systems at the Max Planck Computing and Data Facility. This work was supported in part by the Sherman Fairchild Foundation, and by NSF Grants No. PHY-2309211, No. PHY-2309231, and No. OAC-2209656 at Caltech. A. C. and G. L. acknowledge support from NSF Award No. PHY-2208014, the Dan Black Family Trust and Nicholas and Lee Begovich.

APPENDIX A: COMPARISON WITH A WAVELIKE DRIVER

In this section we compare our accuracy estimates with against a wavelike drive equation of the form of Eq. (18) for the case of Sec. IV A. Similar conclusions as in the main text hold.

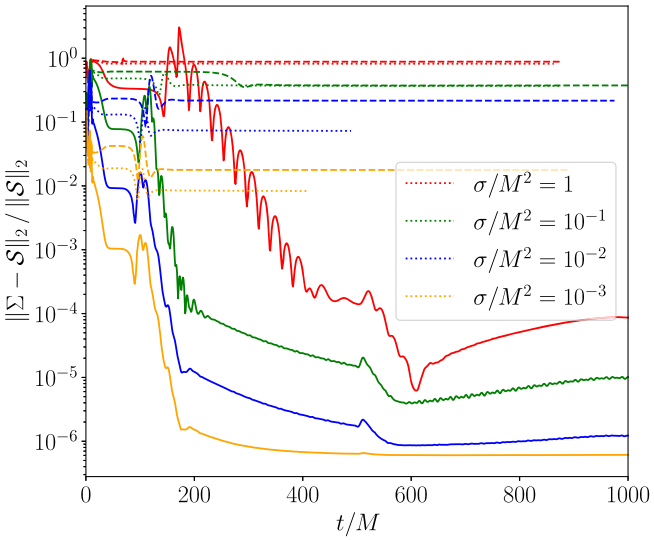

FIG. 9. Comparison of the σ dependence for the relative error the scalar source tracking with a wavelike driver (spinning). Same as Fig. 4 in the main text, but we include the accuracy estimate (dotted lines) for the wavelike driver [Eq. (18)].

In first-order form, the wavelike driver scalar system is given by

$$\begin{aligned}(\partial_t - \beta^i\partial_i)\Sigma &= -\alpha\Pi^{(\Sigma)}\\ (\partial_t - \beta^j\partial_j)\Phi_j^{(\Sigma)} &= -\alpha\partial_i\Pi^{(\Sigma)} - \Pi^{(\Sigma)}\partial_i\alpha + \Phi_j\partial_i\beta^j\\ &\quad + \gamma_2^{(\Sigma)}\alpha(\partial_i\Psi - \Phi_i)\\ \sigma(\partial_t - \beta^i\partial_i)\Pi^{(\Sigma)} &= -\alpha^2\tau\Pi^{(\Sigma)} + \alpha(\Sigma - \mathcal{S}) - \alpha\gamma^{ij}\partial_i\Phi_j^{(\Sigma)}\\ &\quad + \alpha^{(3)}\Gamma^i\Phi_i^{(\Sigma)} + \alpha K\Pi^{(\Sigma)} - \gamma^{ij}\Phi_i^{(\Sigma)}\partial_j\alpha,\end{aligned} \tag{A1}$$

where ${}^{(3)}\Gamma^i \equiv \gamma^{jk\,(3)}\Gamma^i_{jk}$ is a contraction of the spatial Christoffel symbol, $K \equiv \gamma^{ij}K_{ij}$ is the trace of the extrinsic curvature K_{ij}, and $\gamma_{1,2}^{(\Sigma)}$ are parameters which are taken to have the same spatial dependence and value as for the system of the sGB scalar Ψ. Given the similarity of this driver equation to the Klein-Gordon equation, we implement constraint-preserving spherical radiation boundary

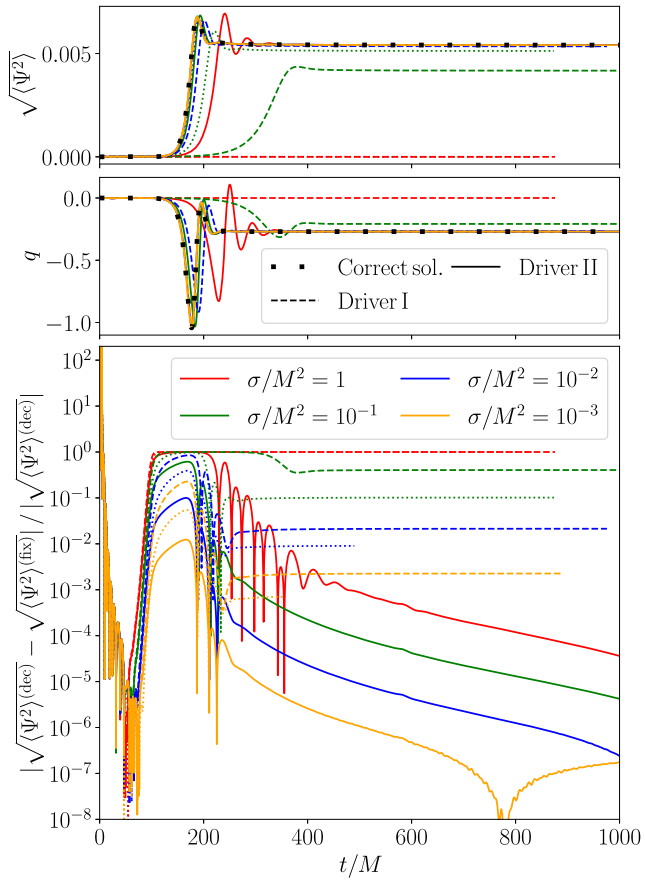

FIG. 10. Comparison of the σ dependence for the relative error of the scalar wave with a wavelike driver (spinning). Same as Fig. 6 in the main text, but extract at $R/M = 50$ and include the accuracy estimate (dotted lines) for the wavelike driver [Eq. (18)].

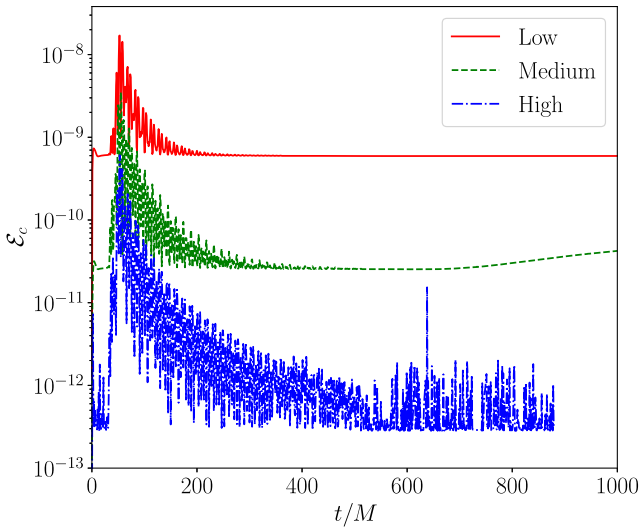

FIG. 11. Convergence test for the constraint energy $\mathcal{E}_c$. The constraint energy [Eq. (53) of Ref. [91]], which combines the $\mathcal{C}_a$, $\mathcal{F}_a, \mathcal{C}_{ab}, \mathcal{C}_{ibc}$, for different p-refinement resolutions. Here $p_{\rm mid} = p_{\rm low} + \Delta p$ and $p_{\rm high} = p_{\rm mid} + \Delta p = p_{\rm low} + 2\Delta p$, for each DG element and direction, with constant increase $\Delta p = 1$.

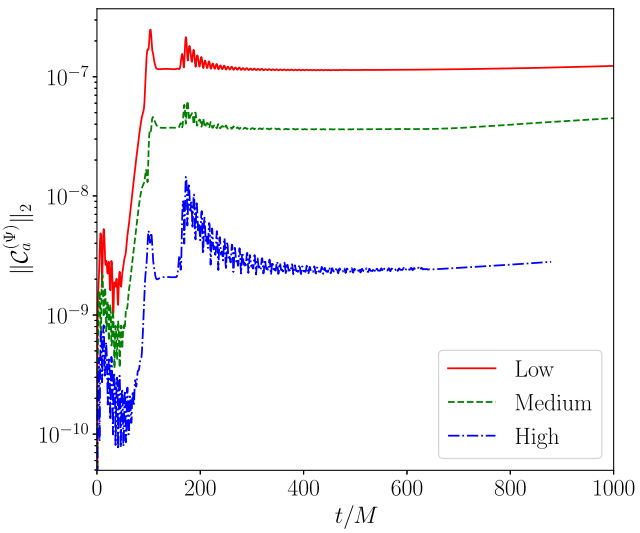

FIG. 12. Convergence test for the one-index constraint $\mathcal{C}_a^{(\Psi)}$. The L_2 norm, in the components and over the spatial grid points, of the $\mathcal{C}_a^{(\Psi)}$ is plotted for different resolutions. Here $p_{\rm mid} = p_{\rm low} + \Delta p$ and $p_{\rm high} = p_{\rm mid} + \Delta p = p_{\rm low} + 2\Delta p$, for each DG element and direction, with constant increase $\Delta p = 1$.

conditions at the outer edge of the domain for this case instead of Dirichlet boundary conditions.

In Fig. 9, we show the relative tracking of the source for all driver equations explored in this work. When using the wavelike driver [Eq. (18)], the solution (in dotted lines) is subject to an asymptotic error with respect to the stationary solution of the decoupling limit. While it improves with respect to driver I [Eq. (16)], it is still outperformed by driver II [Eq. (19)]. In Fig. 10, we show the corresponding accuracy estimate for the scalar wave.

APPENDIX B: CONVERGENCE

In this appendix, we provide more details on the convergence of the simulations presented in the main text.

Since we are using pseudospectral methods to evolve the equations of motion, we expect exponential convergence with increasing number p of basis functions used (p-refinement). In Figs. 11 and 12, we show the convergence of the constraint energy and one-index constraint for Ψ.

[1] J. Aasi *et al.* (LIGO Scientific Collaboration), Advanced LIGO, Classical Quantum Gravity **32**, 074001 (2015).
[2] F. Acernese *et al.* (Virgo Collaboration), Advanced Virgo: A second-generation interferometric gravitational wave detector, Classical Quantum Gravity **32**, 024001 (2015).
[3] T. Akutsu *et al.* (KAGRA Collaboration), Overview of KAGRA: Detector design and construction history, Prog. Theor. Exp. Phys. **2021**, 05A101 (2021).
[4] P. Amaro-Seoane *et al.* (LISA Collaboration), Laser interferometer space antenna, arXiv:1702.00786.
[5] M. Punturo *et al.*, The Einstein Telescope: A third-generation gravitational wave observatory, Classical Quantum Gravity **27**, 194002 (2010).
[6] D. Reitze *et al.*, Cosmic Explorer: The U.S. contribution to gravitational-wave astronomy beyond LIGO, Bull. Am. Astron. Soc. **51**, 035 (2019).
[7] C. M. Will, *Theory and Experiment in Gravitational Physics* (Cambridge University Press, Cambridge, England, 2018).
[8] B. P. Abbott *et al.* (LIGO Scientific and Virgo Collaborations), Tests of general relativity with the binary black hole signals from the LIGO-Virgo catalog GWTC-1, Phys. Rev. D **100**, 104036 (2019).
[9] R. Abbott *et al.* (LIGO Scientific and Virgo Collaborations), Tests of general relativity with binary black holes from the second LIGO-Virgo gravitational-wave transient catalog, Phys. Rev. D **103**, 122002 (2021).
[10] R. Abbott *et al.* (LIGO Scientific, Virgo, and KAGRA Collaborations), Tests of general relativity with GWTC-3, arXiv:2112.06861.
[11] P. Kocherlakota *et al.* (Event Horizon Telescope Collaboration), Constraints on black-hole charges with the 2017

EHT observations of M87*, Phys. Rev. D **103**, 104047 (2021).
[12] K. Akiyama *et al.* (Event Horizon Telescope Collaboration), First Sagittarius A* Event Horizon Telescope results. VI. Testing the black hole metric, Astrophys. J. Lett. **930**, L17 (2022).
[13] M. Crisostomi and K. Koyama, Self-accelerating universe in scalar-tensor theories after GW170817, Phys. Rev. D **97**, 084004 (2018).
[14] D. Langlois and K. Noui, Degenerate higher derivative theories beyond Horndeski: Evading the Ostrogradski instability, J. Cosmol. Astropart. Phys. 02 (2016) 034.
[15] M. Crisostomi, K. Koyama, and G. Tasinato, Extended scalar-tensor theories of gravity, J. Cosmol. Astropart. Phys. 04 (2016) 044.
[16] J. Ben Achour, M. Crisostomi, K. Koyama, D. Langlois, K. Noui, and G. Tasinato, Degenerate higher order scalar-tensor theories beyond Horndeski up to cubic order, J. High Energy Phys. 12 (2016) 100.
[17] G. W. Horndeski, Second-order scalar-tensor field equations in a four-dimensional space, Int. J. Theor. Phys. **10**, 363 (1974).
[18] S. Endlich, V. Gorbenko, J. Huang, and L. Senatore, An effective formalism for testing extensions to general relativity with gravitational waves, J. High Energy Phys. 09 (2017) 122.
[19] S. Weinberg, Effective field theory for inflation, Phys. Rev. D **77**, 123541 (2008).
[20] B. Abbott *et al.* (LIGO Scientific, Virgo, Fermi-GBM, and INTEGRAL Collaborations), Gravitational waves and gamma-rays from a binary neutron star merger: GW170817 and GRB 170817A, Astrophys. J. Lett. **848**, L13 (2017).
[21] B. Abbott *et al.* (LIGO Scientific and Virgo Collaborations), GW170817: Observation of gravitational waves from a binary neutron star inspiral, Phys. Rev. Lett. **119**, 161101 (2017).
[22] P. Creminelli and F. Vernizzi, Dark energy after GW170817 and GRB170817A, Phys. Rev. Lett. **119**, 251302 (2017).
[23] J. M. Ezquiaga and M. Zumalacárregui, Dark energy after GW170817: Dead ends and the road ahead, Phys. Rev. Lett. **119**, 251304 (2017).
[24] T. Baker, E. Bellini, P. G. Ferreira, M. Lagos, J. Noller, and I. Sawicki, Strong constraints on cosmological gravity from GW170817 and GRB 170817A, Phys. Rev. Lett. **119**, 251301 (2017).
[25] J. Sakstein and B. Jain, Implications of the neutron star merger GW170817 for cosmological scalar-tensor theories, Phys. Rev. Lett. **119**, 251303 (2017).
[26] V. Varma, S. E. Field, M. A. Scheel, J. Blackman, L. E. Kidder, and H. P. Pfeiffer, Surrogate model of hybridized numerical relativity binary black hole waveforms, Phys. Rev. D **99**, 064045 (2019).
[27] S. Ossokine *et al.*, Multipolar effective-one-body waveforms for precessing binary black holes: Construction and validation, Phys. Rev. D **102**, 044055 (2020).
[28] G. Pratten *et al.*, Computationally efficient models for the dominant and subdominant harmonic modes of precessing binary black holes, Phys. Rev. D **103**, 104056 (2021).
[29] R. Gamba, S. Akçay, S. Bernuzzi, and J. Williams, Effective-one-body waveforms for precessing coalescing compact binaries with post-Newtonian twist, Phys. Rev. D **106**, 024020 (2022).
[30] T. W. Baumgarte and S. L. Shapiro, *Numerical Relativity: Solving Einstein's Equations on the Computer* (Cambridge University Press, Cambridge England, 2010).
[31] J. Hadamard, Sur les problemes aux derivees partielles et leur signification physique, Princeton Univ. Bull. **13**, 49 (1902).
[32] W. E. East and J. L. Ripley, Dynamics of spontaneous black hole scalarization and mergers in Einstein-scalar-Gauss-Bonnet gravity, Phys. Rev. Lett. **127**, 101102 (2021).
[33] L. Bernard, L. Lehner, and R. Luna, Challenges to global solutions in Horndeski's theory, Phys. Rev. D **100**, 024011 (2019).
[34] J. L. Ripley and F. Pretorius, Gravitational collapse in Einstein dilaton-Gauss–Bonnet gravity, Classical Quantum Gravity **36**, 134001 (2019).
[35] J. L. Ripley and F. Pretorius, Scalarized black hole dynamics in Einstein dilaton Gauss-Bonnet Gravity, Phys. Rev. D **101**, 044015 (2020).
[36] J. L. Ripley and F. Pretorius, Dynamics of a $\mathbb{Z}_2$ symmetric EdGB gravity in spherical symmetry, Classical Quantum Gravity **37**, 155003 (2020).
[37] A. H. K. R, J. L. Ripley, and N. Yunes, Where and why does Einstein-scalar-Gauss-Bonnet theory break down?, Phys. Rev. D **107**, 044044 (2023).
[38] F. Corelli, M. De Amicis, T. Ikeda, and P. Pani, What is the fate of Hawking evaporation in gravity theories with higher curvature terms?, Phys. Rev. Lett. **130**, 091501 (2023).
[39] F. Corelli, M. De Amicis, T. Ikeda, and P. Pani, Non-perturbative gedanken experiments in Einstein-dilaton-Gauss-Bonnet gravity: Nonlinear transitions and tests of the cosmic censorship beyond general relativity, Phys. Rev. D **107**, 044061 (2023).
[40] F. Thaalba, M. Bezares, N. Franchini, and T. P. Sotiriou, Spherical collapse in scalar-Gauss-Bonnet gravity: Taming ill-posedness with a Ricci coupling, Phys. Rev. D **109**, L041503 (2024).
[41] J. L. Ripley, Numerical relativity for Horndeski gravity, Int. J. Mod. Phys. D **31**, 2230017 (2022).
[42] M. Okounkova, L. C. Stein, M. A. Scheel, and D. A. Hemberger, Numerical binary black hole mergers in dynamical Chern-Simons gravity: Scalar field, Phys. Rev. D **96**, 044020 (2017).
[43] M. Okounkova, Stability of rotating black holes in Einstein dilaton Gauss-Bonnet gravity, Phys. Rev. D **100**, 124054 (2019).
[44] M. Okounkova, L. C. Stein, J. Moxon, M. A. Scheel, and S. A. Teukolsky, Numerical relativity simulation of GW150914 beyond general relativity, Phys. Rev. D **101**, 104016 (2020).
[45] M. Okounkova, Numerical relativity simulation of GW150914 in Einstein dilaton Gauss-Bonnet gravity, Phys. Rev. D **102**, 084046 (2020).
[46] H. Witek, L. Gualtieri, P. Pani, and T. P. Sotiriou, Black holes and binary mergers in scalar Gauss-Bonnet gravity: Scalar field dynamics, Phys. Rev. D **99**, 064035 (2019).

[47] H. O. Silva, H. Witek, M. Elley, and N. Yunes, Dynamical descalarization in binary black hole mergers, Phys. Rev. Lett. **127**, 031101 (2021).
[48] M. Elley, H. O. Silva, H. Witek, and N. Yunes, Spin-induced dynamical scalarization, descalarization, and stealthness in scalar-Gauss-Bonnet gravity during a black hole coalescence, Phys. Rev. D **106**, 044018 (2022).
[49] P. Figueras and T. França, Gravitational collapse in cubic Horndeski theories, Classical Quantum Gravity **37**, 225009 (2020).
[50] P. Figueras and T. França, Black hole binaries in cubic Horndeski theories, Phys. Rev. D **105**, 124004 (2022).
[51] M. Bezares, M. Crisostomi, C. Palenzuela, and E. Barausse, K-dynamics: Well-posed $1+1$ evolutions in K-essence, J. Cosmol. Astropart. Phys. 03 (2021) 072.
[52] M. Bezares, L. ter Haar, M. Crisostomi, E. Barausse, and C. Palenzuela, Kinetic screening in nonlinear stellar oscillations and gravitational collapse, Phys. Rev. D **104**, 044022 (2021).
[53] M. Bezares, R. Aguilera-Miret, L. ter Haar, M. Crisostomi, C. Palenzuela, and E. Barausse, No evidence of kinetic screening in simulations of merging binary neutron stars beyond general relativity, Phys. Rev. Lett. **128**, 091103 (2022).
[54] A. Held and H. Lim, Nonlinear dynamics of quadratic gravity in spherical symmetry, Phys. Rev. D **104**, 084075 (2021).
[55] A. Held and H. Lim, Nonlinear evolution of quadratic gravity in $3+1$ dimensions, Phys. Rev. D **108**, 104025 (2023).
[56] M. E. Rubio, A. D. Kovács, M. Herrero-Valea, M. Bezares, and E. Barausse, Well-posed evolution of field theories with anisotropic scaling: The Lifshitz scalar field in a black hole space-time, J. Cosmol. Astropart. Phys. 11 (2023) 001.
[57] A. D. Kovács and H. S. Reall, Well-posed formulation of scalar-tensor effective field theory, Phys. Rev. Lett. **124**, 221101 (2020).
[58] A. D. Kovács and H. S. Reall, Well-posed formulation of Lovelock and Horndeski theories, Phys. Rev. D **101**, 124003 (2020).
[59] W. E. East and J. L. Ripley, Evolution of Einstein-scalar-Gauss-Bonnet gravity using a modified harmonic formulation, Phys. Rev. D **103**, 044040 (2021).
[60] M. Corman, J. L. Ripley, and W. E. East, Nonlinear studies of binary black hole mergers in Einstein-scalar-Gauss-Bonnet gravity, Phys. Rev. D **107**, 024014 (2023).
[61] L. Aresté Saló, K. Clough, and P. Figueras, Well-posedness of the four-derivative scalar-tensor theory of gravity in singularity avoiding coordinates, Phys. Rev. Lett. **129**, 261104 (2022).
[62] L. Aresté Saló, K. Clough, and P. Figueras, Puncture gauge formulation for Einstein-Gauss-Bonnet gravity and four-derivative scalar-tensor theories in $d+1$ spacetime dimensions, Phys. Rev. D **108**, 084018 (2023).
[63] J. Cayuso, N. Ortiz, and L. Lehner, Fixing extensions to general relativity in the nonlinear regime, Phys. Rev. D **96**, 084043 (2017).
[64] N. Deppe *et al.*, SpECTRE (Zenodo, 2024), 10.5281/zenodo.10619885.
[65] G. Allwright and L. Lehner, Towards the nonlinear regime in extensions to GR: Assessing possible options, Classical Quantum Gravity **36**, 084001 (2019).
[66] R. Cayuso and L. Lehner, Nonlinear, noniterative treatment of EFT-motivated gravity, Phys. Rev. D **102**, 084008 (2020).
[67] G. Lara, M. Bezares, and E. Barausse, UV completions, fixing the equations, and nonlinearities in k-essence, Phys. Rev. D **105**, 064058 (2022).
[68] N. Franchini, M. Bezares, E. Barausse, and L. Lehner, Fixing the dynamical evolution in scalar-Gauss-Bonnet gravity, Phys. Rev. D **106**, 064061 (2022).
[69] R. Cayuso, P. Figueras, T. França, and L. Lehner, Modelling self-consistently beyond general relativity, Phys. Rev. Lett. **131**, 111403 (2023).
[70] A. Coates and F. M. Ramazanoğlu, Treatments and placebos for the pathologies of effective field theories, Phys. Rev. D **108**, L101501 (2023).
[71] T. P. Sotiriou and S.-Y. Zhou, Black hole hair in generalized scalar-tensor gravity, Phys. Rev. Lett. **112**, 251102 (2014).
[72] T. P. Sotiriou and S.-Y. Zhou, Black hole hair in generalized scalar-tensor gravity: An explicit example, Phys. Rev. D **90**, 124063 (2014).
[73] R. P. Kerr, Gravitational field of a spinning mass as an example of algebraically special metrics, Phys. Rev. Lett. **11**, 237 (1963).
[74] L. Hui and A. Nicolis, No-hair theorem for the Galileon, Phys. Rev. Lett. **110**, 241104 (2013).
[75] A. Maselli, H. O. Silva, M. Minamitsuji, and E. Berti, Slowly rotating black hole solutions in Horndeski gravity, Phys. Rev. D **92**, 104049 (2015).
[76] P. Creminelli, N. Loayza, F. Serra, E. Trincherini, and L. G. Trombetta, Hairy black-holes in shift-symmetric theories, J. High Energy Phys. 08 (2020) 045.
[77] L. Capuano, L. Santoni, and E. Barausse, Black hole hairs in scalar-tensor gravity and the lack thereof, Phys. Rev. D **108**, 064058 (2023).
[78] D. D. Doneva, F. M. Ramazanoğlu, H. O. Silva, T. P. Sotiriou, and S. S. Yazadjiev, Scalarization, Rev. Mod. Phys. **96**, 015004 (2024).
[79] S. E. Perkins, R. Nair, H. O. Silva, and N. Yunes, Improved gravitational-wave constraints on higher-order curvature theories of gravity, Phys. Rev. D **104**, 024060 (2021).
[80] Z. Lyu, N. Jiang, and K. Yagi, Constraints on Einstein-dilation-Gauss-Bonnet gravity from black hole-neutron star gravitational wave events, Phys. Rev. D **105**, 064001 (2022); Phys. Rev. D **106**, 069901(E) (2022);
[81] M. Herrero-Valea, The shape of scalar Gauss-Bonnet gravity, J. High Energy Phys. 03 (2022) 075.
[82] H. O. Silva, C. F. B. Macedo, T. P. Sotiriou, L. Gualtieri, J. Sakstein, and E. Berti, Stability of scalarized black hole solutions in scalar-Gauss-Bonnet gravity, Phys. Rev. D **99**, 064011 (2019).
[83] H. O. Silva, J. Sakstein, L. Gualtieri, T. P. Sotiriou, and E. Berti, Spontaneous scalarization of black holes and compact stars from a Gauss-Bonnet coupling, Phys. Rev. Lett. **120**, 131104 (2018).

[84] A. Dima, E. Barausse, N. Franchini, and T. P. Sotiriou, Spin-induced black hole spontaneous scalarization, Phys. Rev. Lett. **125**, 231101 (2020).
[85] T. Damour and G. Esposito-Farese, Tensor—scalar gravity and binary pulsar experiments, Phys. Rev. D **54**, 1474 (1996).
[86] D. D. Doneva and S. S. Yazadjiev, New Gauss-Bonnet black holes with curvature-induced scalarization in extended scalar-tensor theories, Phys. Rev. Lett. **120**, 131103 (2018).
[87] G. Antoniou, A. Bakopoulos, and P. Kanti, Evasion of no-hair theorems and novel black-hole solutions in Gauss-Bonnet theories, Phys. Rev. Lett. **120**, 131102 (2018).
[88] M. Minamitsuji and T. Ikeda, Scalarized black holes in the presence of the coupling to Gauss-Bonnet gravity, Phys. Rev. D **99**, 044017 (2019).
[89] C. A. R. Herdeiro, E. Radu, H. O. Silva, T. P. Sotiriou, and N. Yunes, Spin-induced scalarized black holes, Phys. Rev. Lett. **126**, 011103 (2021).
[90] N. A. Wittek *et al.*, Worldtube excision method for intermediate-mass-ratio inspirals: Scalar-field model in $3+1$ dimensions, Phys. Rev. D **108**, 024041 (2023).
[91] L. Lindblom, M. A. Scheel, L. E. Kidder, R. Owen, and O. Rinne, A new generalized harmonic evolution system, Classical Quantum Gravity **23**, S447 (2006).
[92] W. Throwe and S. A. Teukolsky, A high-order, conservative integrator with local time-stepping, arXiv:1811.02499.
[93] A. Bayliss and E. Turkel, Radiation boundary conditions for wave-like equations, Commun. Pure Appl. Math. **33**, 707 (1980).
[94] SXS Collaboration (to be published).
[95] M. A. Scheel, H. P. Pfeiffer, L. Lindblom, L. E. Kidder, O. Rinne, and S. A. Teukolsky, Solving Einstein's equations with dual coordinate frames, Phys. Rev. D **74**, 104006 (2006).
[96] L. Lindblom and B. Szilagyi, An improved gauge driver for the GH Einstein system, Phys. Rev. D **80**, 084019 (2009).
[97] M. W. Choptuik and F. Pretorius, Ultra relativistic particle collisions, Phys. Rev. Lett. **104**, 111101 (2010).
[98] B. Szilagyi, L. Lindblom, and M. A. Scheel, Simulations of binary black hole mergers using spectral methods, Phys. Rev. D **80**, 124010 (2009).
[99] O. Rinne, L. Lindblom, and M. A. Scheel, Testing outer boundary treatments for the Einstein equations, Classical Quantum Gravity **24**, 4053 (2007).
[100] M. A. Scheel, A. L. Erickcek, L. M. Burko, L. E. Kidder, H. P. Pfeiffer, and S. A. Teukolsky, 3-D simulations of linearized scalar fields in Kerr space-time, Phys. Rev. D **69**, 104006 (2004).